

Direct numerical simulation of thermal channel flow for $Re_\tau = 5000$ and $Pr = 0.71$

Francisco Alcántara-Ávila¹, Sergio Hoyas^{1,†} and María Jezabel Pérez-Quiles¹

¹Instituto Universitario de Matemática Pura y Aplicada, Universitat Politècnica de València, Valencia 46022, Spain

(Received 9 April 2020; revised 12 January 2021; accepted 12 March 2021)

A direct numerical simulation of turbulent heat transfer in a channel flow has been conducted for a Reynolds number of 5000 and the Prandtl number of air, 0.71. The mixed boundary condition has been used as the boundary condition of the thermal field. The computational domain has been set to $3.2\pi h$, $2h$ and $1.6\pi h$ in the x , y and z directions, respectively. This domain is large enough to accurately compute the statistics of the flow. Mean values and intensities of the temperature have been obtained. Derived parameters from the average thermal field, such as the von Kármán constant and the Nusselt number have been calculated. An asymptotic behaviour of the von Kármán constant is observed when Re_τ is increased. A correlation for the Nusselt number is proposed. Also, the turbulent Prandtl number has been calculated and it does not present significant changes when Re_τ is increased. Finally, the turbulent budgets are presented. A relation between the increment of the inner peak of the temperature intensities and the scaling failure of the dissipation and viscous diffusion terms is provided. The statistics of all simulations can be downloaded from the web page of our group: <http://personales.upv.es/serhocal/>.

Key words: turbulence simulation, turbulence modelling, turbulence theory

1. Introduction

In the last decades, the computational power of computers has increased exponentially. In the 1990s, the biggest supercomputers reached computing powers of around 100 gigaflops. With the improvement of technology, the performance of computers has increased approximately one order of magnitude every five years. Nowadays, the fastest supercomputers reach computing powers of 200 petaflops. In addition, the use of thousands of processors is relatively easy and efficient. These improvements have allowed researchers to use direct numerical simulations (DNS) for the study of turbulent thermal

[†] Email address for correspondence: serhocal@mot.upv.es

flows during the last three decades. In fact, DNS has proven to be one of the most powerful tools to analyse these types of flows.

Regarding wall turbulence, Poiseuille and Couette flows have been successfully studied through DNS. In recent years, simulations at very high Reynolds numbers have been performed for Poiseuille channel flows. The seminal work of Kim, Moin & Moser (1987) was followed by several authors, increasing the Reynolds number slowly through the years (Moser, Kim & Mansour 1999; Del Alamo *et al.* 2004; Hoyas & Jiménez 2006; Bernardini, Pirozzoli & Orlandi 2014; Lozano-Durán & Jiménez 2014; Lee & Moser 2015). More recently, Yamamoto & Tsuji (2018) computed a $Re_\tau = 8000$ channel flow, which is, to the authors' knowledge, the highest Reynolds number simulated.

Concerning thermal channel flows, the first DNS was performed by Kim & Moin (1987), for $Re_\tau = u_\tau h/\nu \approx 180$ and Prandtl numbers of values $Pr = 0.1, 0.71$ and 2 . Here, u_τ is the friction velocity, h is the half-channel height and ν is the kinematic viscosity. The Prandtl number, Pr , is the ratio of momentum to thermal diffusivity, $Pr = \nu/\alpha$, where α is the thermal diffusion coefficient. In this work, first-order turbulent statistics and correlations between velocity and temperature were obtained. The thermal boundary condition consisted of an internal heat generation that was removed from both cold isothermal walls. This somehow artificial boundary condition is similar to the effect of the pressure term in the momentum equations. After this first work, several more studies of thermal Poiseuille flows were done in the following decade. Different values of Reynolds and Prandtl numbers, and different thermal boundary conditions were used. For example, Lyons, Hanratty & McLaughlin (1991) imposed a temperature difference between both walls; Kasagi, Tomita & Kuroda (1992) used for the first time the mixed boundary condition (MBC). This is a more realistic thermal boundary condition where the average heat flux over both heating walls is constant and the temperature increases linearly in the streamwise direction. The MBC is the thermal condition used in this work. In both works, Lyons *et al.* (1991) and Kasagi *et al.* (1992), the friction Reynolds number used was 150 and the molecular Prandtl number was 0.71 and 1, respectively.

After these basic simulations were performed, using the main three thermal boundary conditions, the trend has been to increase the Reynolds number and to use a wider range of Prandtl numbers. This is due to the fact that the Reynolds numbers, in real life problems, are well above the values used in these works. In the case of the Prandtl number there has been an emphasis on the Prandtl number of air, $Pr = 0.71$, or close to it. The main reason is that an increase of Re_τ and Pr has a computational cost that can be approximated by $L_x^2 L_y Re_\tau^4 Pr^{3/2}$ (Yano & Kasagi 1999), i.e. to simulate water ($Pr \approx 10$) is 50 times more costly than to simulate air. Due to this fact, the highest Reynolds numbers simulated in a DNS of a thermal channel flow using the Prandtl number of air and the MBC has been slowly increasing over time: $Re_\tau = 395$ (Kawamura, Abe & Matsuo 1999); $Re_\tau = 1020$ (Abe, Kawamura & Matsuo 2004); and $Re_\tau = 2000$ (Lluesma-Rodríguez, Hoyas & Peréz-Quiles 2018). Regarding the variation of Prandtl, several works studied the behaviour of the thermal field for lower Prandtl numbers than 0.71. Kasagi & Ohtsubo (1993), performed a study similar to the one in Kasagi *et al.* (1992), but for $Pr = 0.025$. This low Prandtl number is approximately that of mercury. Many other works included this value of 0.025 as a reference of low Prandtl number. For example, Kawamura *et al.* (1998) and then Piller, Nobile & Hanratty (2002) used friction Reynolds numbers 180 and 150, respectively, and studied the thermal field for a wide range of low values of Pr , ranging from 0.025 up to 0.71 and 1, respectively. Kawamura *et al.* (1998) also included an analysis of high values of Prandtl number, up to $Pr = 5$, where the thermal field is more turbulent.

Also for thermal channel flows, but with a different thermal boundary condition, Pirozzoli, Bernardini & Orlandi (2016) reached $Re_\tau = 4000$, using a thermal boundary condition similar to the one in Kim & Moin (1987). A uniform heat generation (UHG) was produced inside the computational box. This value of Re_τ is, up to now, the highest simulated in a DNS of a thermal channel flow. Regarding other kinds of wall flows, a small number of studies have been done for Couette flows and boundary layers. The largest Reynolds numbers simulated have been published in Alcántara-Ávila, Barberá & Hoyas (2019) and Araya & Castillo (2012), respectively.

One of the alternatives to increase the Reynolds number without boosting the computational cost is to reduce the stream and spanwise dimensions of the computational box. However, this computational box needs to have a minimum size to properly describe the flow. This was studied by Lozano-Durán and Jiménez for channel flows (Lozano-Durán & Jiménez 2014) and Lluesma *et al.* for thermal channel flows (Lluesma-Rodríguez *et al.* 2018). In both works, it was found that a computational box of only $2\pi h$ and πh in the streamwise and spanwise directions, respectively, is enough to properly describe the mean flow and the one-point statistics. As is explained below, due to some constraints in the number of points needed by our code, we adopted a slightly larger box of $3.2\pi h \times 2h \times 1.6\pi h$.

To summarize, in this paper, a Reynolds number of 5000 has been simulated for the first time using the MBC. The value of the Prandtl number used is that of air, 0.71. First-order turbulent statistics and turbulent budgets have been obtained and will be discussed.

The structure of the paper is as follows. In the second section, the equations together with the numerical method and the different parameters of each simulation are described. In the third section, the statistics of the temperature fields and the turbulent budgets are discussed. Finally, the fourth section contains the conclusions.

2. Methodology

2.1. Flow configuration and computational domain

The Poiseuille flow described in this work is considered incompressible. The thermal field is treated as a passive scalar. As mentioned before, the boundary condition used for the thermal field is the MBC. For this boundary condition, a uniform heat flux heats both walls, which introduces the heat into the flow. The temperature of these walls increases linearly in the streamwise direction and does not depend on time.

In figure 1, a schematic representation of the lower half of the computational box used can be observed. In this plot, contours of an instantaneous snapshot of the streamwise velocity are represented, coloured by the magnitude of the velocity, and the flow moves from left to right. Periodic conditions are imposed in the streamwise and spanwise boundaries. In previous simulations performed by our group at $Re_\tau = 500$, 1000 and 2000, the computational box dimensions were $2\pi h$, $2h$, πh in the streamwise, wall-normal and spanwise directions, respectively. It was stated in Lozano-Durán & Jiménez (2014) for the flow field, and in Lluesma-Rodríguez *et al.* (2018) for thermal flows, that a computational box with such dimensions is big enough to accurately represent the first-order statistics of the velocity and temperature fields. In order to keep the same resolution for the different Reynolds numbers, the number of collocation points was just multiplied by a factor of two, as was the Reynolds number. However, $Re_\tau = 5000$ is 2.5 times bigger than our closest simulation at $Re_\tau = 2000$. Increasing the number of collocation points only by a factor of two will lead to a poor quality mesh and the results will not be accurate. Since we want to obtain the same mesh resolution as in our previous simulations, the number

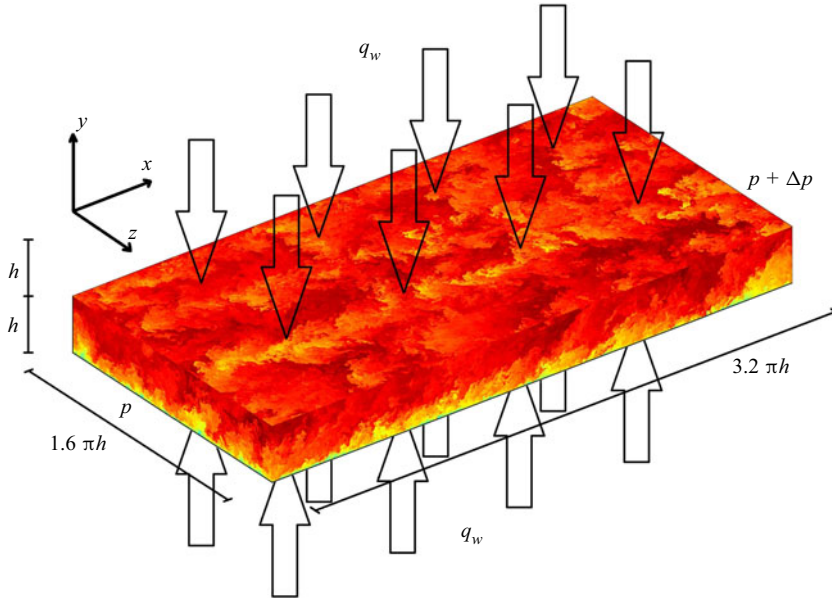


Figure 1. Schematic representation of the lower half of the computational box. The flow is driven by a pressure gradient, ΔP , from left to right. A constant heat flux, q_w , is heating both isothermal walls. Contours represent a snapshot of the streamwise velocity field.

of collocation points in the x and z directions is four times higher than the ones in the simulation of $Re_\tau = 2000$. In order to adjust the mesh resolution, the streamwise and spanwise dimensions have been multiplied by a factor of 1.6. Therefore, on one hand, the computational cost will increase due to the high increase in collocation points. But, on the other hand, since the domain is increased in the periodic directions, the number of statistics obtained every time step also increases. Then, the dimensions of the computational box for the present work are set to $3.2\pi h$, $2h$ and $1.6\pi h$ in the streamwise, wall-normal and spanwise directions, respectively. Coordinates in these directions are denoted by x , y and z , respectively. The corresponding velocities are U , V and W , or, using index notation, U_i . Temperature is represented by T . However, the transformed temperature, Θ (defined below), will be used throughout the entire paper. Uppercase letters denote instantaneous flow magnitudes. Using the Reynolds decomposition, one can obtain the averaged value, denoted by an overbar, and the fluctuating part, denoted by a lowercase letter, of the flow magnitudes, i.e. $U = \bar{U} + u$. The superscript $+$ indicates normalization in wall units, using ν and $u_\tau = \sqrt{\tau_w/\rho}$, where τ_w is the mean shear stress and ρ is the fluid density. The superscript $*$ indicates normalization in outer units, using h and U_b , where U_b is the bulk velocity, i.e. the average velocity in time and space.

2.2. Numerical procedure

The behaviour of turbulent flows is described by the Navier–Stokes equations, which are composed by the continuity and momentum equations,

$$\partial_j U_j^+ = 0, \quad (2.1)$$

$$\partial_t U_i^+ + U_j^+ \partial_j U_i^+ = -\partial_i P^+ + \frac{1}{Re_\tau} \partial_{jj} U_i^+ \quad (2.2)$$

and the energy equation,

$$\partial_t \Theta^+ + U_j^+ \partial_j \Theta^+ = \frac{1}{Re_\tau Pr} \partial_{jj} \Theta^+ + U^+ / \langle U^+ \rangle_{xyz}, \quad (2.3)$$

where $\langle U^+ \rangle_{xyz}$ is the average of U^+ in time and in the three spatial directions, i.e. $\langle U^+ \rangle_{xyz} = U_b^+$. In the energy equation, the transformed temperature, $\Theta = T_w - T$ is used. Since the MBC is used, the temperature in the channel increases linearly in the streamwise direction and periodic conditions cannot be used for T . Here T_w contains the non-periodic part of the temperature, which makes Θ periodic in the streamwise direction. This allows the use of highly efficient Fourier methods in this direction of the channel. In order to perform the simulation, a variation of the code LISO (Hoyas & Jiménez 2006; Hoyas & Jiménez 2008; Avsarkisov *et al.* 2014; Gandía-Barberá *et al.* 2018) has been employed. In this variation, the energy equation was introduced and the code was validated by Lluesma-Rodríguez *et al.* (2018). The method used in LISO to solve the system of (2.1), (2.2) and (2.3) is the same as the one employed in Kim & Moin (1987). For this method, the Navier–Stokes equations are transformed into equations for the wall-normal velocity, Ω_y , and the Laplacian of the wall-normal velocity, Φ . After solving them, the other variables are recovered from these two fields using continuity and vorticity equations. The spatial discretization in the x and z directions is a dealiased Fourier expansion, achieved using the Orszag 2/3 rule (Orszag 1971). In the y direction, the discretization employed is a seven-point compact finite difference scheme with fourth-order consistency and extended spectral-like resolution (Lele 1992). On the other hand, the temporal discretization employs a third-order semi-implicit Runge–Kutta scheme (Spalart, Moser & Rogers 1991).

2.3. Simulation parameters

Table 1 shows the parameters used for the simulation. Information about the dimensionless numbers, the number of collocation points of the mesh and its resolution in every direction and the time of the simulation, is collected. Regarding the resolution of the mesh in the wall-normal direction, the spacing between points has been set to be proportional to the local isotropic Kolmogorov scale $\eta = (v^3/\epsilon)^{1/4}$. The increment in y is set to be $\Delta y = 1.5\eta$. Therefore, the wall-normal resolution obtained, in physical space, is $\Delta y_w^+ = 0.20$ in the walls and $\Delta y_c^+ = 8.1$ in the centreline of the channel. On the other hand, the resolution of the mesh in the streamwise and spanwise directions are $\Delta x^+ \sim 8.18$ and $\Delta z^+ \sim 4.09$, respectively. These values are set to be the same as in Alcántara-Ávila *et al.* (2018) and similar to many other trusted simulations (Kawamura *et al.* 1998; Abe *et al.* 2004; Hoyas & Jiménez 2006; Avsarkisov *et al.* 2014; Lluesma-Rodríguez *et al.* 2018).

In order to initialize the simulation, an initial file of a different case already simulated by our group, at the closest Reynolds number, $Re_\tau = 2000$, and the same Prandtl number, $Pr = 0.71$, has been used. The mean temperature has been approximated extrapolating the temperature fields of the cases $Re_\tau = 1000$ and 2000 , and the velocity field is converged by running the simulation with a coarse mesh. After the transition phase has passed, and once the values of the viscous stress have converged to a plateau, the statistics of the flow were collected. As a first rule of thumb, the simulation was run for at least 10 wash-outs, where a wash-out is the time needed for an eddy to cross the channel (Hoyas & Jiménez 2006). The convergence procedure has been done gradually, increasing in three steps the Reynolds number and then increasing the mesh resolution in one direction at a time. For this reason,

Work	Re_τ	Pr	N_x	N_y	N_z	Δx^+	Δz^+	Δy_w^+	Δy_c^+	tub/L_x
Alcántara-Ávila <i>et al.</i> (2018)	500	0.71	384	251	384	8.18	4.09	0.72	5.3	528
Alcántara-Ávila <i>et al.</i> (2018)	1000	0.71	768	383	768	8.18	4.09	0.44	7.4	130
Alcántara-Ávila <i>et al.</i> (2018)	2000	0.71	1536	633	1536	8.18	4.09	0.32	8.8	47
Pirozzoli <i>et al.</i> (2016)	4088	0.71	10 240	1024	5120	7.5	5.00	0.19	17.7	11
Present	5051	0.71	6144	1685	6144	8.18	4.09	0.20	8.1	12

Table 1. Parameters of the simulation. Columns two and three show the friction Reynolds number and the molecular Prandtl number, respectively. Columns four to six show the number of collocations points on each direction of the computational box, after dealiasing in x and z . In the next four columns, Δ refers to the mesh resolution on each direction and subscripts w and c refer to the walls and the centreline of the channel. The last column shows the time of the simulation in wash-outs.






Work	Re_τ	Thermal B. C.	Line style
Alcántara-Ávila <i>et al.</i> (2018)	500	MBC	
Alcántara-Ávila <i>et al.</i> (2018)	1000	MBC	
Alcántara-Ávila <i>et al.</i> (2018)	2000	MBC	
Pirozzoli <i>et al.</i> (2016)	4088	UHG	
Present	5043	MBC	

Table 2. Line style used to represent each simulation throughout and thermal boundary condition of the case.

the computational cost of the convergence procedure is not negligible compared with the total time of the simulation where the flow is statistically steady.

Through all the paper, the results obtained have been compared with the simulations at the same Prandtl number and lower Reynolds number (2000, 1000 and 500) from Alcántara-Ávila *et al.* (2018). Despite the fact that in the work of Pirozzoli *et al.* (2016) a different thermal boundary condition is used, the Reynolds number used ($Re_\tau = 4000$) is similar to the Re_τ of this paper ($Re_\tau = 5000$). For this reason, a comparison of both works has also been performed. Table 2 shows the colours and line styles that have been used in all figures (unless otherwise specified) to distinguish between each simulation.

In order to confirm that enough statistics have been compiled in the simulation, the heat fluxes have been calculated. These heat fluxes can be obtained from the energy balance equation, which comes from the integration of (2.3),

$$q_{total}^+ = \overbrace{\frac{1}{Pr} \frac{d\bar{\Theta}^+}{dy^+}}^{\text{Molecular}} - \overbrace{v^+ \theta^+}_{\text{Turbulent}} = \overbrace{1 - \frac{1}{Re_\tau} \int_0^{y^+} \frac{U_1^+}{\langle U^+ \rangle_{xyz}} dy^+}^{\text{Total}}. \quad (2.4)$$

Total heat flux has been compared with the molecular and turbulent heat fluxes. It has been considered that enough statistics were obtained when the difference between the left- and right-hand sides of (2.4) was below 10^{-3} . In figure 2(a), all three heat fluxes are represented for the case of $Re_\tau = 5000$. The dotted line represents the difference between the total heat flux and the sum of the molecular and turbulent heat fluxes. It can be seen that this line has a value of almost zero through all the y^+ axis. This indicates that enough statistics of the flow have been gathered. In figure 2(b), the same plot is represented for $Re_\tau = 500, 1000, 2000$ and 5000 . It is observed that the point of crossover between molecular and turbulent heat flux is approximately constant for different

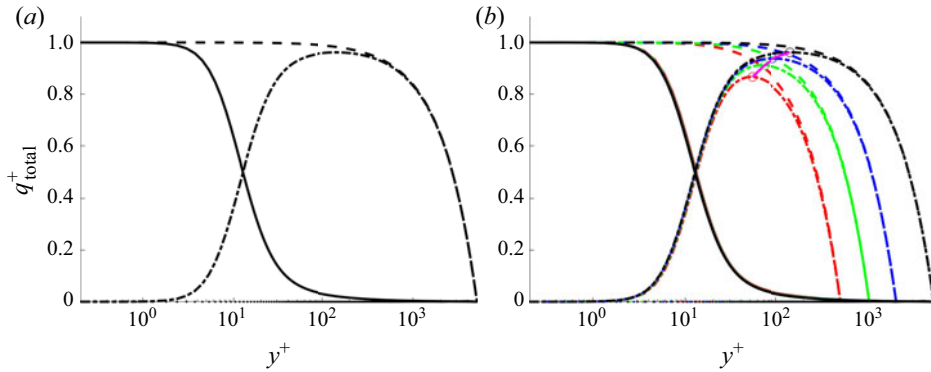


Figure 2. Heat fluxes for (a) $Re_\tau = 5000$ and (b) $Re_\tau = 500, 1000, 2000$ and 5000 : total (dashed); molecular (solid); and turbulent (dash-dotted) heat fluxes. The pointed line represents the difference between the left-hand side and the right-hand side of (2.4). The magenta line represents the maximum molecular heat flux. Colour lines are as in table 2.

Reynolds numbers and it is located at $y^+ \approx 13$. In terms of the y coordinate, this means that the viscous layer is smaller when the Reynolds number is increased, as it should be. In the central region of the channel, the turbulent heat flux increases its maximum value when the Reynolds number is increased. The area below the turbulent heat flux line also increases. All this implies that the thermal flow will be more turbulent for higher Re_τ , as expected.

3. Results

3.1. Temperature statistics

In the present section, the statistics of the simulation have been obtained and they have been analysed and compared with the ones in the works of Pirozzoli *et al.* (2016) and Alcántara-Ávila *et al.* (2018).

The value of the mean temperature, $\bar{\Theta}^+$, has been obtained and it is represented in figure 3(a). As was expected, in the viscous layer, all values of $\bar{\Theta}^+$ collapse with the law of the wall: $\bar{\Theta}^+ = Pr \cdot y^+$. Even the values from Pirozzoli *et al.* (2016), where a different boundary condition for the thermal field is used, coincide with the ones obtained in the present work. This shows the universality of turbulence near the wall. However, in the logarithmic layer and in the central region of the channel, the slope of $\bar{\Theta}^+$ tends to decrease with the Reynolds number. For the UHG boundary condition used in Pirozzoli *et al.* (2016), the slope is smaller than the one obtained using the MBC.

One parameter that is derived from the mean temperature profile is the von Kármán constant, κ_t . In the logarithmic layer, $\bar{\Theta}^+$ can be estimated with a logarithmic equation

$$\bar{\Theta}^+ = \frac{1}{\kappa_t} \ln(y^+) + B. \quad (3.1)$$

The range of validity of (3.1) has been chosen to be $y^+ > 70$ and $y^+ < 0.2Re_\tau$, as suggested by Jiménez (2013). Therefore, in this range, κ_t represents the inverse of the slope of $\bar{\Theta}^+$. This von Kármán constant has been considered independent of the Reynolds number, the type of flow and the boundary conditions by many researchers (Jiménez 2018). The values of κ_t are represented in figure 3(b). Results at lower Reynolds numbers from the work of Pirozzoli *et al.* (2016) have also been added (magenta circles). In addition, the

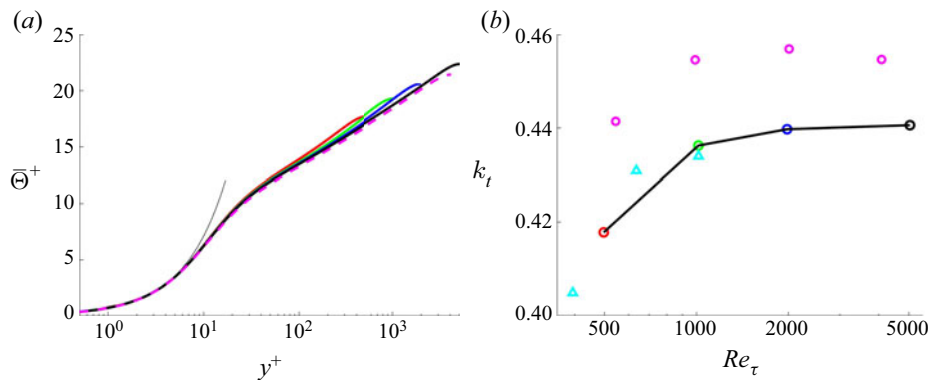


Figure 3. (a) Mean temperature; the black thin line shows the law of the wall. (b) Here κ_t as a function of Re_τ ; magenta circles represents the data from Pirozzoli *et al.* (2016); cyan triangles are the data from Abe *et al.* (2004), where the MBC is used, as in this work. Lines are as in table 2.

Re_τ	κ_t	B	κ_∞	α_1	κ	α_2
500	0.418	2.89	—	—	—	—
1000	0.436	3.11	0.4625	150	0.433	1.304
2000	0.440	3.05	0.4635	150	0.448	1.436
5000	0.441	2.96	0.4466	150	0.441	0.756
4000	0.455	3.09	0.4651	150	0.457	0.961

Table 3. Values of the parameters of (3.1) and (3.3).

values of κ_t obtained in Abe *et al.* (2004) are represented with cyan triangles. In the work of Abe *et al.* (2004), the same boundary condition as in this work, the MBC, was used. Results are coherent among all different works.

Here, it is seen that κ_t slightly increases with Re_τ , but, asymptotically, tends to a value slightly above 0.44. One may think that κ_t depends on the Reynolds number. However, the reason for the variations in the value of κ_t is that the logarithmic region is not properly developed and it is influenced by the buffer layer and the outer region. A value of $\kappa_t = 0.441$ is obtained for $Re_\tau = 5000$. This value is slightly above the von Kármán constant of the velocity field, which ranges between 0.38 and 0.4 (Lozano-Durán & Jiménez 2014; Lee & Moser 2015). With respect to the UHG, the value of κ_t increases to 0.455, since the slope of $\bar{\Theta}^+$ is lower, as it was mentioned before. Regarding the constant B from (3.1), their values are collected in table 3. Notice that this more or less constant value of $B \approx 3$ obtained in all simulations is totally different when the Prandtl number changes (Alcántara-Ávila *et al.* 2018).

A visual way of checking how well developed the logarithmic layer is, can be by using the diagnostic function, β , defined as

$$\beta = y \partial_y \bar{\Theta}^+. \quad (3.2)$$

If (3.1) holds, then the diagnostic function will have a value of $1/\kappa_t$ in the logarithmic layer. In figure 4(a), the diagnostic function of the mean temperature is represented. This logarithmic layer appears between the two peaks of the diagnostic function that are obtained in the buffer layer and the outer region. Regarding the peak in the buffer layer, its position is constant at $y^+ \approx 12$ and its magnitude continues decreasing with the increase of

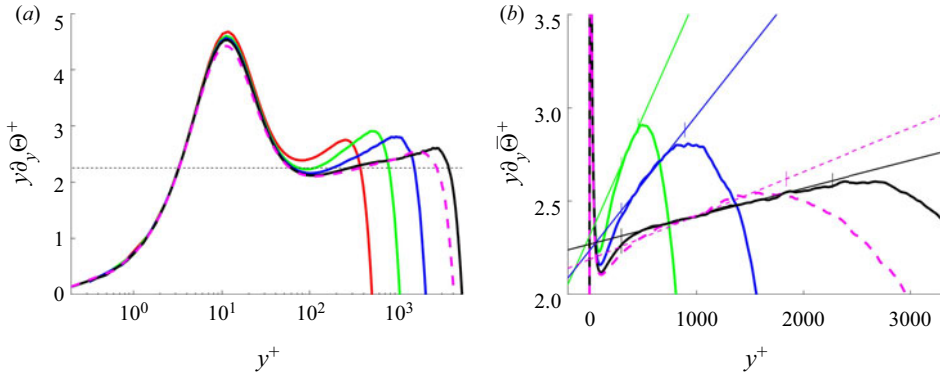


Figure 4. (a) Here κ_t as a function of Re_τ ; the dotted black line represents where the plateau should be for $\kappa_t = 0.44$. (b) Diagnostic functions (solid) and approximations of (3.3) (dashed). Colours are as in table 2.

the Reynolds number. This peak is even lower for the UHG boundary condition. Regarding the peak in the outer region, it is positioned at a constant value in outer coordinates, $y/h \approx 0.5$. In the ideal case where a logarithmic region appears perfectly developed, a plateau of value $1/\kappa_t$ should be observed approximately between $y^+ > 70$ and $y/h < 0.2$. This is not observed in any of the cases, since β increases along the logarithmic layer. However, it is true that the slope of β tends to zero as the Reynolds number increases. This indicates that higher Reynolds numbers must be simulated in order to be able to find a plateau in the logarithmic layer.

This problem was addressed by Jiménez & Moser (2007). They studied this influence of the Reynolds number in the slope of β on the logarithmic region for the mean velocity profile, U^+ . They used a higher-order truncation in which the diagnostic function had the form

$$\beta = y \partial_y \bar{U}^+ = \overbrace{\left(\frac{1}{\kappa_\infty} + \frac{\alpha_1}{Re_\tau} \right)}^{1/\kappa} + \alpha_2 \frac{y^+}{Re_\tau}, \quad (3.3)$$

where the Reynolds number dependence is introduced in the term κ and a linear dependence with y/h is introduced in the term y^+/Re_τ . This approximation was valid in the range $y^+ > 300$ and $y/h < 0.45$. The same analysis has been performed here for $\bar{\Theta}^+$. Note that the case $Re_\tau = 500$ does not appear in this analysis since the range where the approximation is valid does not exist. In figure 4(b), a zoom of the diagnostic function together with the approximations of (3.3) are represented.

Values of the parameters of the approximation are presented in table 3. The value of α_1 has been set to 150 as in Jiménez & Moser (2007). While κ and κ_t seem to be more or less converged, α_2 is still larger than the expected limit value of zero for high Reynolds number.

Another parameter that can be derived from the mean thermal field is the Nusselt number, Nu . According to Kawamura *et al.* (1998), Nu can be computed as

$$Nu = \frac{Lh}{\kappa} = \frac{2Re_\tau Pr}{\langle \Theta_m^+ \rangle}, \quad (3.4)$$

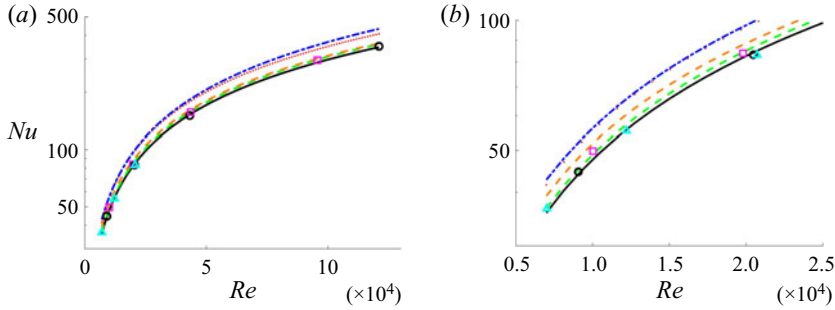


Figure 5. (a) Nusselt number as a function of Re . (b) Zoom for the lower Reynolds numbers. Black circles represent the data from Alcántara-Ávila *et al.* (2018) and from this work, magenta squares are the data from Pirozzoli *et al.* (2016) and cyan triangles are the data from Abe *et al.* (2004). Lines represent correlations: black solid (3.6); red dotted Dittus & Boelter (1930) (3.7); orange dashed Gnielinski (1976) (3.8); green dashed Kays *et al.* (1980) (3.9); and blue dotted-dashed Sleicher & Rouse (1975) (3.10).

where $\langle \Theta_m^+ \rangle$ is defined as

$$\langle \Theta_m^+ \rangle = \frac{\int_0^1 U^+ \Theta^+ dy^*}{\int_0^1 U^+ dy^*}, \quad (3.5)$$

and h is the convective heat transfer coefficient. In figure 5, the obtained Nusselt numbers, as a function of Re , are presented. In the range of Reynolds numbers studied, the Nusselt number can be approximated with a power function of Re ,

$$Nu = 0.031 Re^{0.796} \quad \text{for } Pr = 0.71, \quad (3.6)$$

where the coefficient of determination is $R^2 = 0.99976$, with $R^2 = 1$ representing a perfect fit. The data has been compared with results from Pirozzoli *et al.* (2016) at lower Reynolds numbers and from Abe *et al.* (2004). Also, four correlations have been used to compare them with correlation (3.6). Two of them are correlations for turbulent flows in pipes: Dittus & Boelter (1930)

$$Nu = 0.023 Re_D^{0.8} Pr^n; \quad (3.7)$$

and Gnielinski (1976)

$$Nu = \frac{(f/8)(Re_D - 1000)Pr}{1 + 12.7(f/8)^{1/2}(Pr^{2/3} - 1)}; \quad (3.8)$$

where Re_D is the diameter of the pipe, n is a coefficient of value 0.4 since the fluid is being heated and f is proportional to the skin friction coefficient, $f = (0.79 \ln(Re_D) - 1.64)^{-2}$. On the other hand, two correlations for constant temperature walls are used. The Kays, Crawford & Weigand (1980) correlation reads

$$Nu = 0.021 Re^{0.8} Pr^{0.5} \quad (3.9)$$

and the Sleicher & Rouse (1975) correlation

$$Nu = 4.8 + 0.0156 Re^{0.85} Pr^{0.93} \quad \text{for } Pr < 0.1. \quad (3.10)$$

On one hand, figure 5(a) presents a global image, with all the Reynolds numbers that are being analysed in this work, including the ones from Abe *et al.* (2004) and Pirozzoli *et al.* (2016). Figure 5(b) presents a zoom in the low Reynolds numbers for a better view

DNS of thermal channel flow

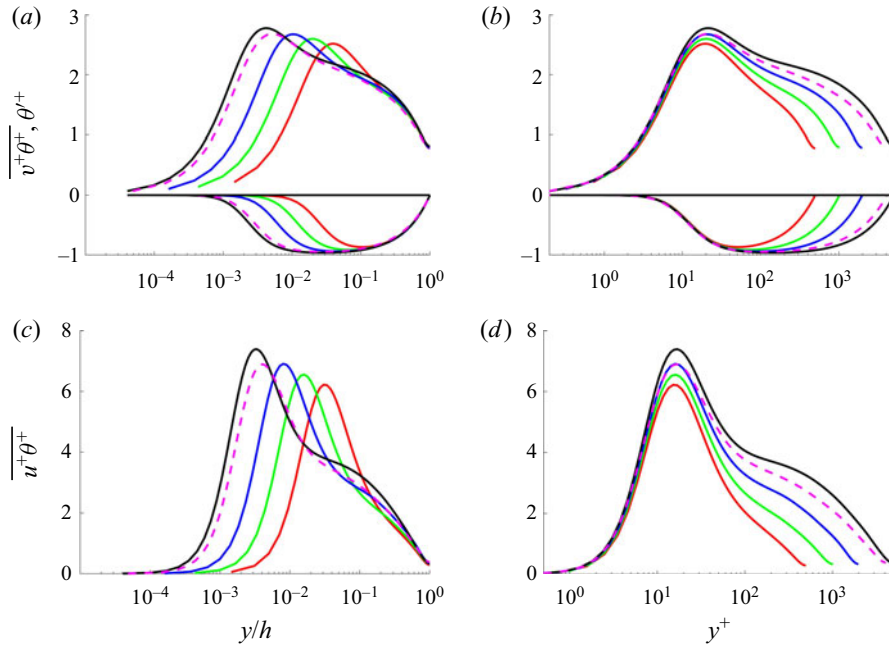


Figure 6. Here θ'^+ and $\overline{v^+\theta'^+}$ in (a) outer coordinates and (b) inner coordinates. Here also $\overline{u^+\theta'^+}$ in (c) outer coordinates and (d) inner coordinates. Lines are as in table 2.

of the discrepancies between different boundary conditions and correlations in this range of Re .

One can see that the Nusselt number obtained in Abe *et al.* (2004) follows the same trend as the ones obtained in this work, since the MBC is employed in both cases. However, Nu in Pirozzoli *et al.* (2016) is slightly higher, since the magnitude of the mean temperature is lower when the UHF thermal condition is used. In other words, the convective heat transfer is lower when the MBC is used.

Regarding the correlations, the ones from Dittus & Boelter (1930) (3.7) and Sleicher & Rouse (1975) (3.10) overestimate the value of Nu , either because it is for turbulent pipes or because the correlation is valid for lower Prandtl numbers. Correlations from Gnielinski (1976) (3.8) and Kays *et al.* (1980) (3.9) adjust much better to the result obtained. They perfectly adjust to the result from Pirozzoli *et al.* (2016). Anyway, note that the exponent of Re from correlations (3.7), (3.9) and (3.10) is (or it is close to) 0.80, which is also the case for the correlation proposed in this work (3.6). It is a future work to propose a correlation that also includes the effect of the Prandtl number.

Turbulent intensities are represented in figure 6. The root mean square of the temperature variance, θ'^+ , and the wall-normal heat flux, $\overline{v^+\theta'^+}$, are represented in figures 6(a) and 6(b) as a function of outer and inner coordinates, respectively. Also, streamwise heat flux, $\overline{u^+\theta'^+}$, is represented in figures 6(c) and 6(d) as a function of outer and inner coordinates, respectively.

The main result is that a perfect collapse of the statistics is observed in the inner layer, when the plot is represented in inner coordinates, figures 6(b) and 6(d). On the other hand, when the statistics are represented as a function of the outer coordinates, the collapse is observed in the outer region of the channel.

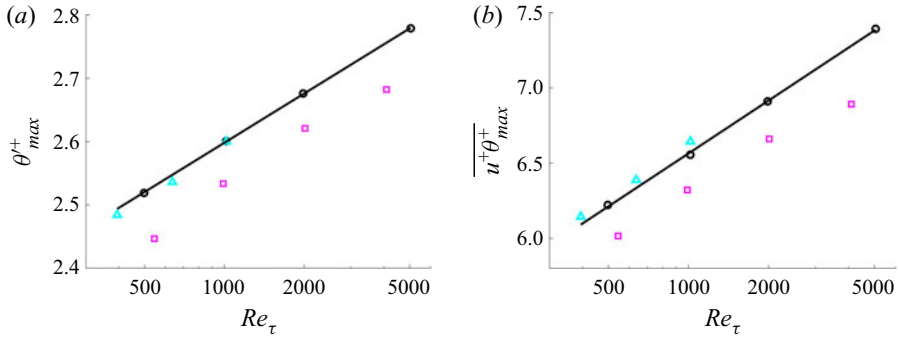


Figure 7. Maximum value of (a) θ'^+ and (b) $\overline{u^+\theta^+}$, both as a function of Re_τ . Black line represents correlation (3.11) in (a) and correlation (3.12) in (b). The black circles, data from this work and from Alcántara-Ávila *et al.* (2018); magenta squares, Pirozzoli *et al.* (2016); and cyan triangles, Abe *et al.* (2004).

The maximum values of the turbulent intensities θ'^+ and $\overline{u^+\theta^+}$ occur in the buffer layer. Their values can be observed in figures 7(a) and 7(b). The peaks increase with Reynolds number, which indicates a more turbulent flow, as was expected. Here θ'^+ and $\overline{u^+\theta^+}$ present a linear increase with respect to $\log(Re_\tau)$. Values of the peaks can be obtained with the following correlations:

$$\theta'^+_{max} = 0.112 \log(Re_\tau) + 1.82, \quad (3.11)$$

$$\overline{u^+\theta^+}_{max} = 0.508 \log(Re_\tau) + 3.06. \quad (3.12)$$

On the other hand, $\overline{v^+\theta^+}$ does not present this linear increase. The peak occurs in the outer region and its value increases slowly as the Reynolds number increases. This was already shown in the magenta line of figure 2(b). Actually, $\overline{v^+\theta^+}$ is bounded by -1 , as can be observed from (2.4). The maximum value of q^+_{total} is 1. The turbulent heat flux has its maximum in the core region of the channel. The higher the Reynolds number is, the closer to 1 the value of q^+_{total} will be in this core region. Since in this region $q^+_{total} \approx -\overline{v^+\theta^+}$, for very high Reynolds numbers $-\overline{v^+\theta^+}$ will be close to 1.

Regarding the UHG case, the peaks of the three intensities have a lower absolute value, which indicates a less turbulent thermal field than the one obtained using the MBC. Lower Reynolds number cases have been also represented to see how this feature happens for all simulations, obtaining the same tendency. Also, data from Abe *et al.* (2004) has been added. This has been done to verify the results, since Abe *et al.* (2004) also used the MBC. Effectively, the results are very similar, and the small differences (less than 1 %) can be due to numerical discrepancies or different mesh resolution.

In a similar way that the mean velocity and temperature are studied through the diagnostic function in the logarithmic layer, velocity intensities can be analysed through Townsend's attached eddy hypothesis (Townsend 1976). This hypothesis is valid for high Reynolds number flows, in a certain region of y , where the velocity intensities satisfy

$$u'^2 = A_1 - B_1 \log(y/h), \quad (3.13)$$

$$v'^2 = A_2, \quad (3.14)$$

DNS of thermal channel flow

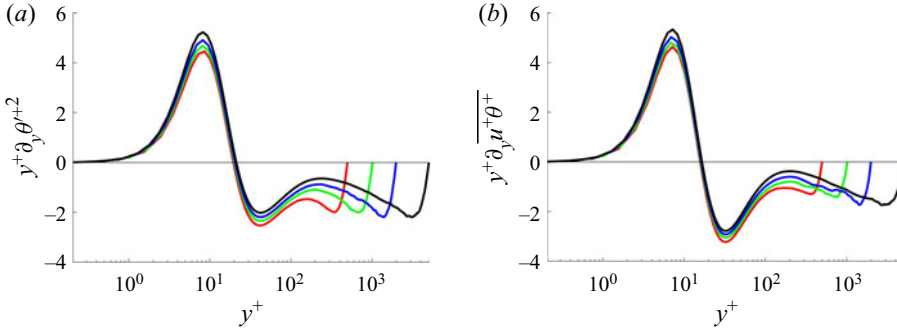


Figure 8. Diagnostic function for (a) θ'^{2+} and (b) $\overline{u'\theta'^+}$. Lines are as in table 2.

$$w'^{2+} = A_3 - B_3 \log(y/h), \quad (3.15)$$

$$\overline{u'v'^+} = -1. \quad (3.16)$$

Analogously, due to the high correlation between u'^{+} and θ'^{+} , one may think that Townsend's hypothesis is valid for the thermal field when u'^{+} is replaced by θ'^{+} . Doing this, the following relations are obtained:

$$\theta'^{2+} = A_4 - B_4 \log(y/h), \quad (3.17)$$

$$\overline{u'\theta'^+} = A_5 - B_6 \log(y/h), \quad (3.18)$$

$$\overline{v'\theta'^+} = -1. \quad (3.19)$$

It has already been shown that the minimum value of $\overline{v'\theta'^+}$ tends to -1 in a wider range of y/h when the Reynolds number is increased (figures 6a and 6b). This is in accordance with (3.19). Regarding θ'^{2+} and $\overline{u'\theta'^+}$, their diagnostic functions can be observed in figures 8(a) and 8(b), respectively. If Townsend's criteria can be applied to the thermal field, there should be a plateau in the $y^+ \partial_y \theta'^{2+}$ and $y^+ \partial_y \overline{u'\theta'^+}$ profiles. For these values of Re_τ there is no evidence of this plateau, although the trends may indicate that for higher Reynolds numbers it may appear in the logarithmic layer.

Another important parameter for modelling of thermal flows is the turbulent Prandtl number, Pr_t . It is defined as the ratio between the momentum eddy diffusivity, ν_t , to the thermal eddy diffusivity, κ_t ,

$$Pr_t = \frac{\nu_t}{\kappa_t} = \frac{\overline{uv} \, d\bar{\Theta}/dy}{\overline{v\theta} \, d\bar{U}/dy}. \quad (3.20)$$

In figure 9, Pr_t is shown as a function of y^+ . In the viscous layer, it can be seen how Pr_t is close to 1 and constant for all values of Reynolds numbers. This confirms the well known law that states $Pr_t \approx 1$ in the wall for medium molecular Prandtl numbers (Kawamura *et al.* 1998; Alcántara-Ávila *et al.* 2018). Some differences are observed with respect to the Pr_t obtained by Pirozzoli *et al.* (2016). However, in the buffer layer and logarithmic region, all values of Pr_t seem to collapse, including the ones obtained in Pirozzoli *et al.* (2016). In the outer layer, values of Pr_t decrease. In conclusion, there have not been observed new behaviours of the turbulent Prandtl number for the Reynolds number $Re_\tau = 5000$.

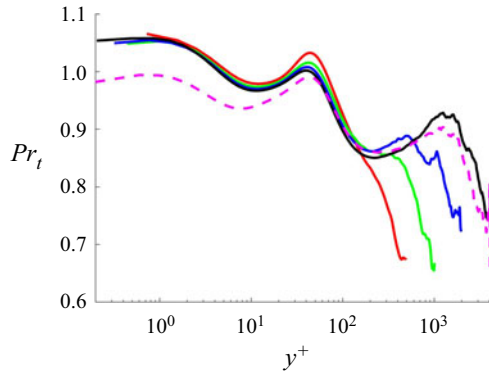


Figure 9. Turbulent Prandtl number. Lines are as in table 2.

3.2. Turbulent budgets

In this section, budgets of the temperature variance, $k_\theta = 1/2\overline{\theta^2}$, the dissipation rate of the temperature variance, $\varepsilon_\theta = (1/Pr)\overline{\partial_i\theta\partial_i\theta}$ and the turbulent heat fluxes, $\overline{u\theta}$ and $\overline{v\theta}$, are presented. The equation for the budget of k_θ is

$$\frac{Dk_\theta}{Dt} = P + T + V + \varepsilon_\theta, \quad (3.21)$$

where D/Dt is the mean substantial derivative and P is the production term, T is the turbulent diffusion, V is the viscous diffusion and ε_θ is the dissipation term. Each term is defined as follows:

$$P = -\overline{v\theta}\partial_y\bar{\Theta}, \quad (3.22)$$

$$T = -\frac{1}{2}\partial_y\overline{\theta^2v}, \quad (3.23)$$

$$V = \frac{1}{2Pr}\partial_{yy}^2\overline{\theta^2}, \quad (3.24)$$

$$\varepsilon_\theta = -\frac{1}{Pr}\overline{\partial_i\theta\partial_i\theta}. \quad (3.25)$$

For ε_θ , the following budget equation is obtained:

$$\frac{D\varepsilon_\theta}{Dt} = P_m + P_{mg} + P_g + P_t + T_t + V_{\varepsilon_\theta} + \varepsilon_{\theta 1}, \quad (3.26)$$

where P_m , P_{mg} , P_g and P_t are the mixed production, mean gradient production, gradient production and turbulent production, respectively. Here T_t , V_{ε_θ} and $\varepsilon_{\theta 1}$ are the turbulent diffusion, molecular diffusion and dissipation terms. Their definitions are given by

$$P_m = -\frac{2}{Pr}\overline{\partial_i v \partial_i \theta \partial_y \bar{\Theta}}, \quad (3.27)$$

$$P_{mg} = -\frac{2}{Pr}\overline{\partial_x \theta \partial_y \bar{\theta} \partial_y \bar{U}}, \quad (3.28)$$

$$P_g = -\frac{2}{Pr}\overline{v \partial_y \theta \partial_{yy}^2 \bar{\Theta}}, \quad (3.29)$$

DNS of thermal channel flow

$$P_t = -\frac{2}{Pr} \overline{\partial_i \theta \partial_j \theta \partial_j u_i}, \quad (3.30)$$

$$T_t = -\frac{1}{Pr} \partial_y \overline{v \partial_i \theta \partial_i \theta}, \quad (3.31)$$

$$V_{\varepsilon_\theta} = \frac{1}{Pr^2} \partial_{yy}^2 \varepsilon_0, \quad (3.32)$$

$$\varepsilon_{\theta 1} = -\frac{2}{Pr^2} \overline{\partial_{kj}^2 \theta \partial_{kj}^2 \theta}. \quad (3.33)$$

Finally, the budget equations for the turbulent heat fluxes are

$$\frac{Du_i \bar{\theta}}{Dt} = P_i + T_i + V_i + \Pi_i^s + \Pi_i^d + \varepsilon_i, \quad (3.34)$$

where each term, from left to right, is the production, turbulent diffusion, viscous diffusion, pressure–temperature gradient correlation, pressure diffusion and dissipation. These terms are defined as

$$P_i = -\overline{u_i v} \partial_y \bar{\theta} - \overline{v \theta} \partial_y \overline{U_i}, \quad (3.35)$$

$$T_i = -\partial_{x_k} \overline{u_i u_k \theta}, \quad (3.36)$$

$$V_i = \nu \partial_{x_k} \left(\overline{\theta \partial_{x_k} u_i} + \frac{1}{Pr} \overline{u_i \partial_{x_k} \theta} \right), \quad (3.37)$$

$$\Pi_i^s = \overline{p \partial_{x_i} \theta}, \quad (3.38)$$

$$\Pi_i^d = -\partial_{x_k} (\delta_{ki} \overline{p \theta}), \quad (3.39)$$

$$\varepsilon_i = -\nu \left(1 + \frac{1}{Pr} \right) \overline{\partial_{x_k} u_i \partial_{x_k} \theta}, \quad (3.40)$$

where δ_{ij} is Kronecker's delta and repeated index implies summation over $k = 1, 2, 3$.

Figure 10 shows the different budget terms for all cases that use the MBC in table 2. Figure 10(a) represents the budget terms of k_θ . The term $\nu/u_\tau^2 \theta_\tau^2$ has been used to normalize the data. In figure 10(b), the budgets of ε_θ are represented. For these budget terms, $\nu^3/u_\tau^4 \theta_\tau^2$ have been used for the normalization. In addition, the four production terms of ε_θ have been added. This summation has been represented as a single production term to facilitate the visualization and interpretation. Finally, figures 10(c) and 10(d) show the budget terms of $\overline{u\theta}$ and $\overline{v\theta}$, respectively. These data have been normalized by $\nu/u_\tau^3 \theta_\tau$. The idea of this section is to study if these normalizations, proposed in Lluesma-Rodríguez *et al.* (2018) and Kozuka, Seki & Kawamura (2009), work for the different Re_τ so that the data collapse in all the channels.

For k_θ , figure 10(a), all terms collapse for $y^+ > 10$. In the buffer layer, the turbulent diffusion terms present small discrepancies between all cases. Furthermore, in the viscous layer there are big differences between each viscous diffusion and the dissipation terms. The absolute values of these terms increase with the Reynolds number.

The reason for the discrepancies in the wall for the viscous diffusion and the dissipation terms can be understood by doing a Taylor series approximation as in

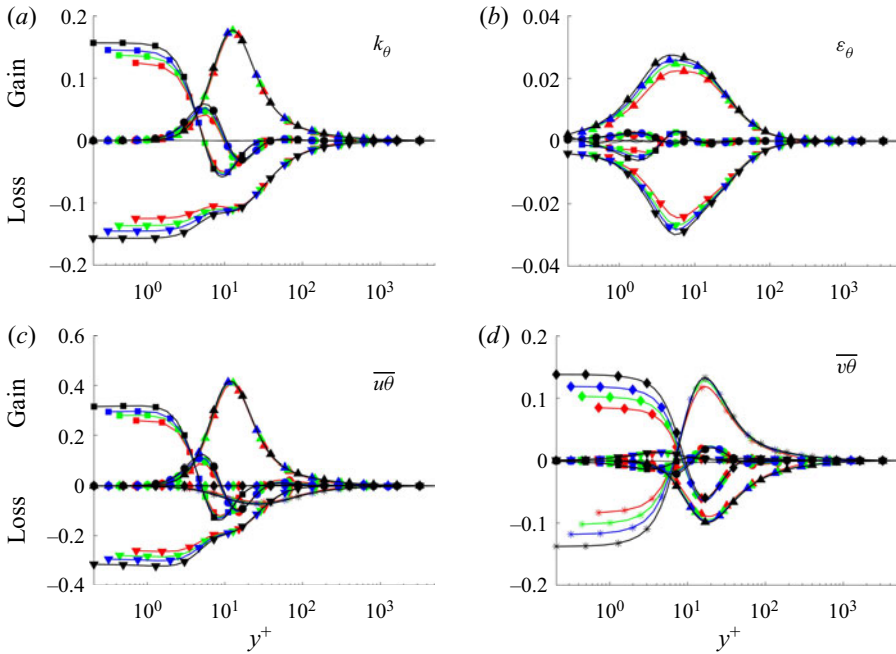


Figure 10. Budgets of (a) temperature variance, $\overline{k_\theta}$, (b) dissipation rate of the temperature variance, $\overline{\varepsilon_\theta}$, (c) streamwise heat flux, $\overline{u\theta}$ and (d) wall-normal heat flux, $\overline{v\theta}$. Symbols denote budget terms: production or sum of productions in panel (b), (triangle up); turbulent diffusion (circle); viscous diffusion (square); dissipation (triangle down); pressure strain (star); and pressure diffusion (diamond). The black line with value 0 is the summation of all terms. Lines are as in table 2.

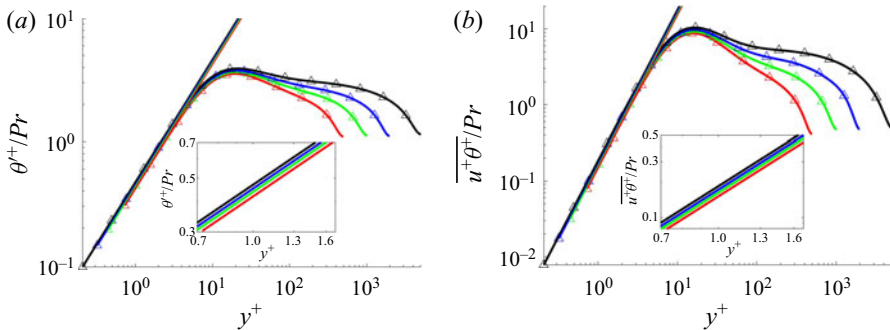


Figure 11. (a) Here θ'^+/Pr and (b) $\overline{u'^+\theta'^+}/Pr$ in wall coordinates. Zooms of the viscous layer. Lines are as in table 2.

Kawamura *et al.* (1998). Here θ'^+ can be approximated by

$$\theta'^+ = Pr(b_\theta y^+ + c_\theta y^{+2} + \dots). \quad (3.41)$$

Therefore, near the wall, $\theta'^+ \approx Pr \cdot b_\theta \cdot y^+$. In figure 11(a) it is shown how this is true for approximately $y^+ < 3$. The values of b_θ are collected in table 4.

Re_τ	b_θ	$V^+ _{y=0}$	$Pr \cdot b_\theta^2$
500	0.4202	0.1246	0.1254
1000	0.4385	0.1360	0.1365
2000	0.4529	0.1449	0.1456
5000	0.4692	0.1565	0.1563

Table 4. First column shows the case. Values of b_θ are in second column. Third and fourth columns show the value of $V^+|_{y=0}$ obtained from the statistics and calculated with (3.43), respectively.

On the other hand, one can approximate the value of the viscous diffusion term, V , in the wall as follows:

$$V|_{y=0} = \frac{1}{2Pr} \partial_{yy} \overline{\theta'^2} \Big|_{y=0}. \quad (3.42)$$

Using approximation (3.41), the value of V in the wall is

$$V^+|_{y=0} \approx Pr \cdot b_\theta^2. \quad (3.43)$$

The result of the approximation is almost the actual value (table 4). In all cases the error is lower than 1 %. Therefore, the reason why this term of the turbulent budget does not scale in the wall comes from the differences in the b_θ terms. This term represents the slope of θ'^+/Pr near the wall. Looking at the zoom in figure 11(a), one can see that, effectively, the lines of θ'^+/Pr are parallel, but they do not collapse. The differences in V for cases with the same Prandtl number is due to the increase in the slope of θ'^+ with the Reynolds number. One may think that this value of b_θ converges for very large Reynolds numbers, as it may look from the trend in table 4. However, it was seen in figure 6(b) that the maximum value of θ'^+ always increases with Re_τ , at least for $Re_\tau \leq 5000$. Because the position of the peak was constant in y^+ , the slope of θ'^+ has to be higher for larger Re_τ . In other words, as long as the peak of θ'^+ increases with Re_τ , b_θ will also increase and V cannot scale at the wall. It was observed in Alcántara-Ávila & Hoyas (2020), that for high Prandtl numbers, the peak value of θ'^+ was approximately constant, which yielded an approximately constant value of b_θ and, therefore, a much better scaling of the viscous diffusion term near the wall. This suggests that the effect of reaching a constant behaviour of θ'^+ in the near-wall region, and thus, a good scaling of V^+ at the wall, only depends on the thermal field. The same analysis can be done for the dissipation term, since, at the wall, $V = -\varepsilon_\theta$.

In the case of ε_θ (figure 10b) the scaling failures appear in the buffer layer for the sum of production terms and the dissipation. This increase of the production terms was already reported in other works such as Abe & Antonia (2009).

For the budgets of $\overline{u\theta}$ (figure 10c), the viscous diffusion and dissipation terms do not scale near the wall, like in $\overline{k_\theta}$. Actually, the phenomenon is very similar and it can be studied in the same way. The streamwise velocity fluctuation and heat flux can be approximated as in Kawamura *et al.* (1998),

$$u'^+ = b_1 y^+ + c_1 y^{+2} + \dots, \quad (3.44)$$

$$\overline{u^+ \theta'^+} = Pr \left(b_{1\theta} y^{+2} + c_{1\theta} y^{+3} + \dots \right). \quad (3.45)$$

Re_τ	$b_{1\theta}$	$V_u^+ _{y=0}$	$(Pr+1)b_{1\theta}$
500	0.1512	0.2562	0.2586
1000	0.1619	0.2717	0.2768
2000	0.1713	0.2853	0.2930
5000	0.1836	0.3138	0.3139

Table 5. First column shows the case. Values of $b_{1\theta}$ are in second column. Third and fourth columns show the value of $V_u^+|_{y=0}$ obtained from the statistics and calculated with (3.51), respectively.

Therefore, near the wall, $u'^+ \approx b_{1\theta}y^+$ and $\overline{u^+\theta^+} \approx Pr \cdot b_{1\theta} \cdot y^{+2}$. The approximation is shown for $\overline{u^+\theta^+}$ in figure 11(b). It presents a good estimation up to $y^+ < 4$. A similar picture was obtained for u'^+ with good agreement for $y^+ < 3$, not shown for brevity. The viscous diffusion of $\overline{u\theta}$, V_u , has the following form at the wall:

$$V_u|_{y=0} = \nu \partial_y \left(\overline{\theta \partial_y u} + \frac{1}{Pr} \overline{u \partial_y \theta} \right) \Big|_{y=0}. \quad (3.46)$$

Using the chain rule, we obtain

$$V_u|_{y=0} = \nu \left(\overline{\partial_y \theta \partial_y u} + \overline{\partial_y \partial_{yy} u} \right) \quad (3.47)$$

$$+ \frac{1}{Pr} \overline{\partial_y u \partial_y \theta} + \frac{1}{Pr} \overline{u \partial_{yy} \theta} \Big|_{y=0}. \quad (3.48)$$

Since $\overline{\theta \partial_{yy} u} = \overline{u \partial_{yy} \theta} = 0$ at the wall, one gets

$$V_u|_{y=0} = \nu \frac{Pr+1}{Pr} \left(\overline{\partial_y \theta \partial_y u} + \overline{\partial_y u \partial_y \theta} \right) \Big|_{y=0} \quad (3.49)$$

$$= \nu \frac{Pr+1}{Pr} \partial_{yy} \overline{u\theta} \Big|_{y=0}. \quad (3.50)$$

Using the definition from (3.45) we finally obtain

$$V_u^+|_{y=0} = (Pr+1) b_{1\theta}. \quad (3.51)$$

For $V_u^+|_{y=0}$ the errors are lower than 3 % for all cases (see table 5), proving a good accuracy of the approximation. Therefore, while $b_{1\theta}$ increases with the Reynolds number, the value of V_u^+ will also increase at the wall. This will occur as long as the peak of $\overline{u^+\theta^+}$ keeps increasing (figure 6d).

As a conclusion, the scaling failure near the wall of V^+ and V_u^+ is due to the increase of the peak of θ'^+ and $\overline{u^+\theta^+}$, respectively.

Regarding the turbulent budgets of $\overline{v^+\theta^+}$ (figure 10d), small scaling failures appear in the buffer layer for the production and pressure strain terms. Near the wall, bigger discrepancies appear for the pressure strain and pressure diffusion terms. The pressure strain term can be written as

$$\Pi_v^s = \overline{p \partial_y \theta}. \quad (3.52)$$

The reason why Π_v^s does not scale in the wall is again because the term $\overline{p \partial_y \theta}$ has a peak at a constant y^+ and it continuously increases with the Reynolds number; not shown here for brevity.

DNS of thermal channel flow

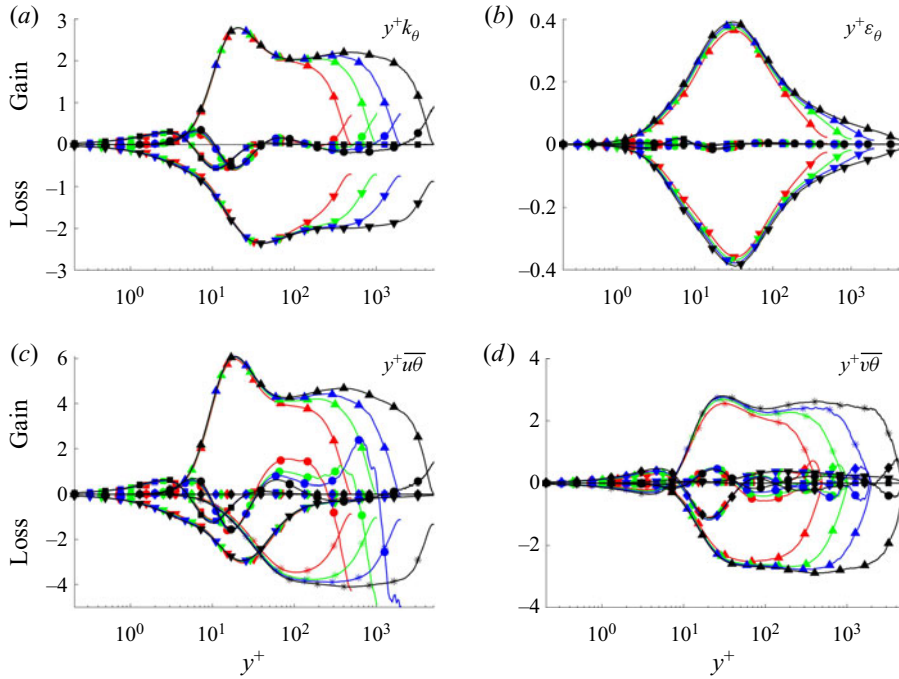


Figure 12. Budgets of the y^+ -premultiplied (a) temperature variance, $y^+ \overline{k_\theta}$, (b) dissipation rate of the temperature variance, $y^+ \overline{\varepsilon_\theta}$, (c) streamwise heat flux, $y^+ \overline{u\theta}$ and (d) wall-normal heat flux, $y^+ \overline{v\theta}$. Symbols denote budget terms: production or sum of productions in (b), (triangle up); turbulent diffusion (circle); viscous diffusion (square); dissipation (triangle down); pressure strain (star); and pressure diffusion (diamond). The black line with value 0 is the summation of all terms. Lines are as in table 2.

As a general comment, the budgets of $\overline{k_\theta}$ and $\overline{u^+ \theta^+}$ are very similar due to the high correlation between u'^+ and θ'^+ . Near the wall, the energy enters the thermal flow through viscous diffusion and it is extracted by dissipation. Also, the peak of the production term is constant for different Reynolds numbers. For $\overline{k_\theta}$, the value of P is $Pr/4$, as noted by Abe & Antonia (2017). On the other hand, there is not a clear scaling with Pr for the peak of P_1 . In the case of the budgets of $\overline{v^+ \theta^+}$, a similar picture to that of $\overline{u^+ v^+}$ is obtained (not shown here for brevity), again, due to the high correlation between u'^+ and θ'^+ . In this case, the energy is introduced by the pressure strain and it is extracted by the pressure diffusion.

A different picture is obtained above the buffer layer, up to approximately $y/h = 0.4$. Figure 12 shows the same turbulent budgets as before, premultiplied by y^+ . In a perfectly developed logarithmic layer, the kinetic energy production scales with $1/y^+$ (Hoyas & Jiménez 2008). Note that this is approximately true for the dominant budgets of $\overline{k_\theta}$, $\overline{u\theta}$ and $\overline{v\theta}$. Therefore, a much better comparison between the dominant budget terms above the buffer layer can be done. As in the near-wall region, production is the dominant budget term of $\overline{k_\theta}$, which is compensated by the dissipation term. However, in the case of $\overline{u\theta}$, and also for $\overline{v\theta}$, it is the pressure strain what compensates the production term.

In the centre of the channel (above $y/h = 0.4$) the velocity and temperature flatten and all production terms tend to zero. Turbulent diffusion becomes the dominant budget of $\overline{k_\theta}$ and it is compensated by the dissipation.

As a final comment, there are no noticeable changes in the behaviour of the turbulent budgets with respect to lower Reynolds number cases. In the present study all cases analysed had the same Prandtl number. However, the value of b_θ and $b_{1\theta}$ decrease drastically for $Pr \leq 0.2$ (Kawamura *et al.* 1998). In Alcántara-Ávila *et al.* (2018) the effects of low Prandtl numbers on the scaling were shown. A similar analysis of the turbulent budgets for high Prandtl numbers is reported in Alcántara-Ávila & Hoyas (2020).

4. Conclusions

A DNS of a thermal channel flow at $Re_\tau = 5000$ has been conducted for the first time. The MBC has been used. The Prandtl number of air, 0.71, was used. The results obtained are compared with other simulations using the same Prandtl number and lower Reynolds numbers: $Re_\tau = 500$, 1000 and 2000. Also, the simulation with closest Reynolds number, $Re_\tau = 4000$, is used to compare results. In that simulation the UHG boundary condition was used. A comparison between both boundary conditions is provided.

The mean temperature is calculated and its diagnostic function still does not show a plateau in the logarithmic layer. Higher Reynolds numbers are needed in order to properly study the behaviour of the thermal field in this logarithmic region. The von Kármán constant presents an asymptotic behaviour with an increasing Reynolds number and it tends to converge at a value of approximately 0.44. The reason why κ_t is not constant is attributed to the influence of the inner and outer regions on the logarithmic region, since for these Reynolds numbers this logarithmic region is small. This effect of the Reynolds number on the logarithmic layer is also studied through a slightly different diagnostic function. For this case, a new term that contemplates the dependence of the Reynolds number is introduced. Effectively, the value of this term tends towards zero when the Reynolds number is increased.

A new correlation for the Nusselt number is provided. This correlation is valid for turbulent thermal channel flows, $Pr = 0.71$ and $500 \leq Re_\tau \leq 5000$. It has been compared with classical Nusselt number correlations. Regarding the turbulent Prandtl number, there are not relevant results at $Re_\tau = 5000$ and the trends of Pr_t are the same as for lower Reynolds numbers.

Thermal intensities increase with the Reynolds number and the values of the inner peaks increase logarithmically with Re_τ for θ'^+ and $\overline{u^+\theta^+}$. Here $\overline{v^+\theta^+}$ tends to have a minimum value close to -1 in a wider range of y^+ for high Reynolds numbers. This agrees with the application of Townsend's hypotheses to the thermal intensities. However, θ'^{+2} and $\overline{u^+\theta^+}$ do not present a logarithmic dependence at any region of y as it indicates Townsend's hypotheses. A remarkable difference between the MBC and UHF thermal conditions is observed in the temperature intensities. Magnitudes of these intensities are higher when the MBC is used, meaning that a more turbulent flow is obtained.

Turbulent budgets are presented and scaling failures are analysed. The most relevant scaling failures are the ones that occur near the wall for the dissipation and viscous diffusion terms of k_θ and $\overline{u\theta}$. These scaling failures are a direct result of the increase of the inner peak of θ'^+ and $\overline{u^+\theta^+}$, respectively. In the cases of the budgets of $\overline{v^+\theta^+}$, the scaling failures occur in the pressure strain and pressure diffusion terms. In the same way, this occurs for the increase of the inner peak of the variable $\overline{p^+\partial_y\theta^+}$.

Availability of data. The raw data that support the findings of this study are available from the corresponding author upon reasonable request. One point statistics can be downloaded from the web page of our group: <http://personales.upv.es/serhocal/>

Acknowledgements. This work was supported by RTI2018-102256-B-I00 of MINECO/FEDER. F.A.A. is partially funded by GVA/FEDER project ACIF2018. The computations of the new simulations were made possible by a generous grant of computing time from the Barcelona Supercomputing Centre, reference IM-2019-3-0021. We are grateful to Messrs Kawamura, Pirozzoli, Bernardini and Orlandi for providing us with copies of their original data.

Declaration of interests. The authors report no conflict of interest.

Author ORCIDs.

 Francisco Alcántara-Ávila <https://orcid.org/0000-0003-0704-6100>;

 Sergio Hoyas <https://orcid.org/0000-0002-8458-7288>.

REFERENCES

- ABE, H. & ANTONIA, R.A. 2009 Turbulent Prandtl number in a channel flow for $Pr = 0.025$ and 0.71 . In *Proceedings of the 6th International Symposium on Turbulence and Shear Flow Phenomena* (ed. R. Friedrich & A.V. Johansson), vol. 1, pp. 67–72. Seoul National University.
- ABE, H. & ANTONIA, R.A. 2017 Relationship between the heat transfer law and the scalar dissipation function in a turbulent channel flow. *J. Fluid Mech.* **830**, 300–325.
- ABE, H., KAWAMURA, H. & MATSUO, Y. 2004 Surface heat-flux fluctuations in a turbulent channel flow up to $Re_\tau = 1020$ with $Pr = 0.025$ and 0.71 . *Intl J. Heat Fluid Flow* **25** (3), 404–419.
- ALCÁNTARA-ÁVILA, F., BARBERÁ, G. & HOYAS, S. 2019 Evidences of persisting thermal structures in couette flows. *Intl J. Heat Fluid Flow* **76**, 287–295.
- ALCÁNTARA-ÁVILA, F. & HOYAS, S. 2020 Direct numerical simulation of thermal channel flow for medium–high Prandtl numbers up to $Re_\tau = 2000$. *Intl J. Heat Mass Transfer* (submitted).
- ALCÁNTARA-ÁVILA, F., HOYAS, S. & PÉREZ-QUILES, M.J. 2018 DNS of thermal channel flow up to $Re_\tau = 2000$ for medium to low Prandtl numbers. *Intl J. Heat Mass Transfer* **127**, 349–361.
- ARAYA, G. & CASTILLO, L. 2012 DNS of turbulent thermal boundary layers up to $Re_\theta = 2300$. *Intl J. Heat Mass Transfer* **55**, 4003–4019.
- AVSARKISOV, V., HOYAS, S., OBERLACK, M. & GARCÍA-GALACHE, J.P. 2014 Turbulent plane Couette flow at moderately high Reynolds number. *J. Fluid Mech.* **751**, R1.
- BERNARDINI, M., PIROZZOLI, S. & ORLANDI, P. 2014 Velocity statistics in turbulent channel flow up to $Re_\tau = 4000$. *J. Fluid Mech.* **758**, 327–343.
- DEL ALAMO, J.C., JIMÉNEZ, J., ZANDONADE, P. & MOSER, R.D. 2004 Scaling of the energy spectra of turbulent channels. *J. Fluid Mech.* **500**, 135–144.
- DITTUS, F.W. & BOELTER, L.M.K. 1930 *Heat Transfer in Automobile Radiators of the Tubular Type*. Publications in Engineering, vol. 2, no. 13, pp. 443–461. University of California Press.
- GANDÍA-BARBERÁ, S., HOYAS, S., OBERLACK, M. & KRAHEBERGER, S. 2018 The link between the Reynolds shear stress and the large structures of turbulent Couette-Poiseuille flow. *Phys. Fluids* **30** (4), 041702.
- GNIELINSKI, V. 1976 New equations for heat and mass transfer in turbulent pipe and channel flow. *Intl Chem. Engng* **16**, 359–367.
- HOYAS, S. & JIMÉNEZ, J. 2006 Scaling of the velocity fluctuations in turbulent channels up to $Re_\tau = 2003$. *Phys. Fluids* **18** (1), 011702.
- HOYAS, S. & JIMÉNEZ, J. 2008 Reynolds number effects on the Reynolds-stress budgets in turbulent channels. *Phys. Fluids* **20** (10), 101511.
- JIMÉNEZ, J. 2013 Near-wall turbulence. *Phys. Fluids* **25** (10), 101302.
- JIMÉNEZ, J. 2018 Coherent structures in wall-bounded turbulence. *J. Fluid Mech.* **842**, P1.
- JIMÉNEZ, J. & MOSER, R.D. 2007 What are we learning from simulating wall turbulence? *Phil. Trans. R. Soc. Lond. A* **365**, 715–732.
- KASAGI, N. & OHTSUBO, Y. 1993 Direct numerical simulation of low Prandtl number thermal field in a turbulent channel flow. In *Turbulent Shear Flows* (ed. F. Durst, R. Friedrich, B.E. Launder, F.W. Schmidt, U. Schumann & J.H. Whitelaw), vol. 8, pp. 97–119. Springer.
- KASAGI, N., TOMITA, Y. & KURODA, A. 1992 Direct numerical simulation of passive scalar field in a turbulent channel flow. *Trans. ASME J. Heat Transfer* **114** (3), 598–606.
- KAWAMURA, H., ABE, H. & MATSUO, Y. 1999 DNS of turbulent heat transfer in channel flow with respect to Reynolds and Prandtl number effects. *Intl J. Heat Fluid Flow* **20**, 196–207.
- KAWAMURA, H., OHSAKA, K., ABE, H. & YAMAMOTO, K. 1998 DNS of turbulent heat transfer in channel flow with low to medium-high Prandtl number fluid. *Intl J. Heat Fluid Flow* **19** (5), 482–491.

- KAYS, W.M., CRAWFORD, M.E. & WEIGAND, B. 1980 *Convective Heat and Mass Transfer*. McGraw-Hill.
- KIM, J. & MOIN, P. 1987 Transport of passive scalars in a turbulent channel flow. *NASA 1* (TM-89463), 1–14.
- KIM, J., MOIN, P. & MOSER, R. 1987 Turbulence statistics in fully developed channels flows at low Reynolds numbers. *J. Fluid Mech.* **177**, 133–166.
- KOZUKA, M., SEKI, Y. & KAWAMURA, H. 2009 DNS of turbulent heat transfer in a channel flow with a high spatial resolution. *Intl J. Heat Fluid Flow* **30** (3), 514–524.
- LEE, M. & MOSER, R. 2015 Direct numerical simulation of turbulent channel flow up to $Re_\tau \approx 5200$. *J. Fluid Mech.* **774**, 395–415.
- LELE, S.K. 1992 Compact finite difference schemes with spectral-like resolution. *J. Comput. Phys.* **103** (1), 16–42.
- LLUESMA-RODRÍGUEZ, F., HOYAS, S. & PERÉZ-QUILES, M.J. 2018 Influence of the computational domain on DNS of turbulent heat transfer up to $Re_\tau = 2000$ for $Pr = 0.71$. *Intl J. Heat Mass Transfer* **122**, 983–992.
- LOZANO-DURÁN, A. & JIMÉNEZ, J. 2014 Effect of the computational domain on direct simulations of turbulent channels up to $Re_\tau = 4200$. *Phys. Fluids* **26** (1), 011702.
- LYONS, S.L., HANRATTY, T.J. & MCLAUGHLIN, J.B. 1991 Direct numerical simulation of passive heat transfer in a turbulent channel flow. *Intl J. Heat Mass Transfer* **34** (4–5), 1149–1161.
- MOSER, R.D., KIM, J. & MANSOUR, N.N. 1999 Direct numerical simulation of turbulent channel flow up to $Re_\tau = 590$. *Phys. Fluids* **11** (4), 943–945.
- ORSZAG, S.A. 1971 On the elimination of aliasing in finite difference schemes by filtering high-wavenumber components. *J. Atmos. Sci.* **28**, 1074.
- PILLER, M., NOBILE, E. & HANRATTY, T.J. 2002 DNS study of turbulent transport at low Prandtl numbers in a channel flow. *J. Fluid Mech.* **458**, 419–441.
- PIROZZOLI, S., BERNARDINI, M. & ORLANDI, P. 2016 Passive scalars in turbulent channel flow at high Reynolds number. *J. Fluid Mech.* **788**, 614–639.
- SLEICHER, C.A. & ROUSE, M.W. 1975 A convenient correlation for heat transfer to constant and variable property fluids in turbulent pipe flow. *Intl J. Heat Mass Transfer* **18**, 677–683.
- SPALART, P.R., MOSER, R.D. & ROGERS, M.M. 1991 Spectral methods for the Navier–Stokes equations with one infinite and two periodic directions. *J. Comput. Phys.* **96** (2), 297–324.
- TOWNSEND, A.A. 1976 *The Structure of Turbulent Shear Flows*, 2nd ed. Cambridge University Press.
- YAMAMOTO, Y. & TSUJI, Y. 2018 Numerical evidence of logarithmic regions in channel flow at $Re_\tau = 8000$. *Phys. Rev. Fluids* **3**, 012602(R).
- YANO, T. & KASAGI, N. 1999 Direct numerical simulation of turbulent heat transport at high Prandtl numbers. *JSME Intl J. B* **42** (2), 284–292.